Supporting Information

Molecular Dynamics and Structural Studies of Zinc Chloroquine Complexes

Mirko Paulikat[a,††], Daniele Vitone[b, ††], Florian K. Schackert[a,c, ††], Nils Schuth[d, ††], Alessandra Barbanente[b], GiovanniMaria Piccini[e], Emiliano Ippoliti[a], Giulia Rossetti[a,f,g], Adam H. Clark[h], Maarten Nachtegaal[h], Michael Haumann[i], Holger Dau[i], Paolo Carloni[a,c,*], Silvano Geremia[j], Rita De Zorzi[j], Liliana Quintanar[d], Fabio Arnesano[b]

[a] Computational Biomedicine (IAS-5/INM-9), Forschungszentrum Jülich GmbH, 52428 Jülich, Germany

[b] Department of Chemistry, University of Bari "Aldo Moro", 70125 Bari, Italy

[c] Department of Physics, RWTH Aachen University, 52062 Aachen, Germany

[d] Department of Chemistry, Center for Research and Advanced Studies (Cinvestav), 07360 Mexico City, Mexico

[e] Euler Institute, Università della Svizzera italiana, 6962 Lugano, Switzerland

[f] Jülich Supercomputing Centre (JSC), Forschungszentrum Jülich GmbH, 52428 Jülich, Germany

[g] Department of Neurology, RWTH Aachen University, 52062 Aachen, Germany

[h] Paul Scherrer Institute, 5232 Villigen, Switzerland

[i] Department of Physics, Freie Universität Berlin, 14195 Berlin, Germany

[j] Department of Chemical and Pharmaceutical Sciences, University of Trieste, 34127 Trieste, Italy

* Email: p.carloni@fz-juelich.de

1. NMR AND MS

1.1 Methods

Electrospray ionization mass spectrometry (ESI-MS) experiments. Sample aliquots of free ligand and zinc complexes in DMSO-d_6 solutions were diluted with 20 mM ammonium chloride buffer and infused into the mass spectrometer, an Agilent 6530 Accurate-Mass Quadruple Time-of-Flight (Q-TOF) system equipped with an electrospray interface. Ionization was achieved in the positive or negative ion mode by application of 4.0 kV at the entrance of the capillary; the pressure of the nebulizer gas was 20 psi. The drying gas was heated to 325 °C at a flow rate of 10 µL/min. Full-scan mass spectra were recorded in the mass/charge (m/z) range of 50–3000. Isotopic distributions were calculated with the program Molecular Weight Calculator (https://omics.pnl.gov/software/molecular-weightcalculator).

1.2 Results

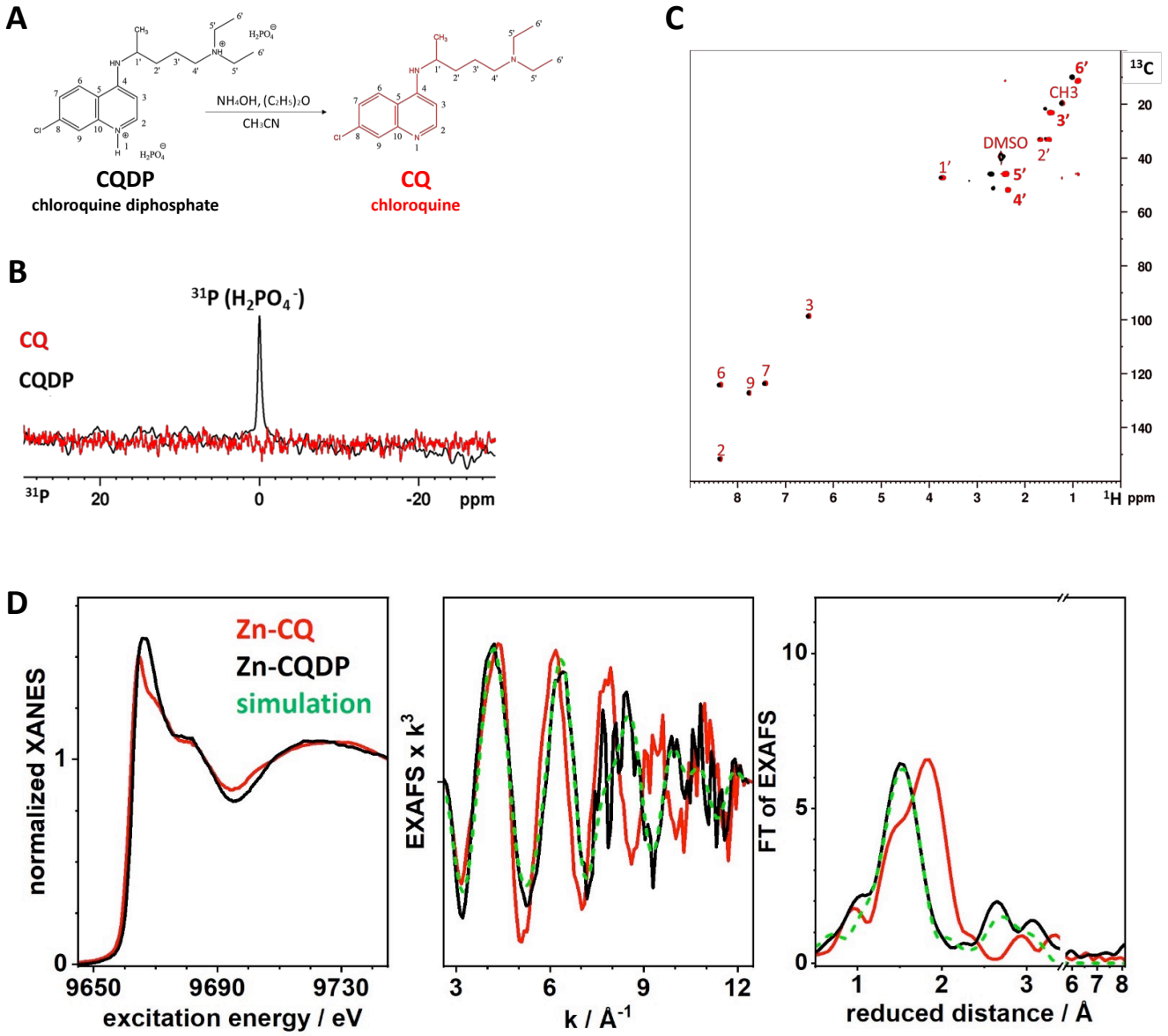

Figure S1. (A) Extraction protocol of chloroquine (CQ) from its diphosphate salt (CQDP). (B) Superposition of 1D ^{31}P and (C) 2D ^{1}H-^{13}C HSQC NMR spectra of CQDP (black) and free CQ (red) in DMSO-d_6. The cross-peaks are labeled according to the atom numbering shown on the chemical structures in panel (A). (D) Zn K-edge X-ray absorption spectroscopy (XAS) of Zn-CQ (red) and Zn-CQDP frozen in DMSO-d_6. Shown are normalized X-ray absorption near edge structure (XANES; left), extended X-ray absorption fine structure (EXAFS; center) and Fourier transform of EXAFS (right). Green dashed line corresponds to the EXAFS fit for the spectrum of Zn-CQDP using simulation parameters given in Table S3. The EXAFS fit for the Zn-CQ complex in DMSO is shown in Figure 4. The Zn-CQDP complex was prepared as described by Navarro *et al.*[1]

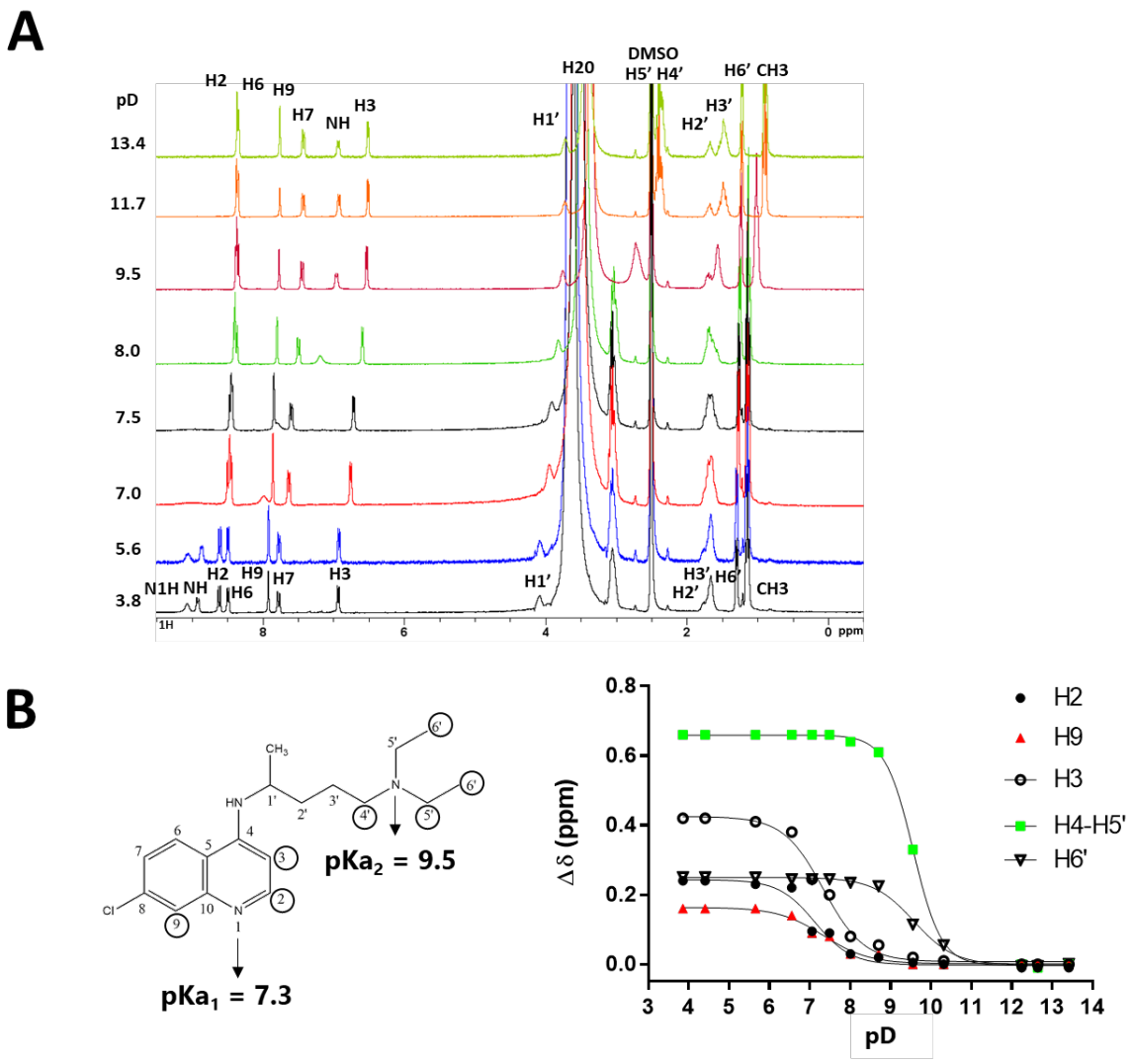

Figure S2. (A) 1D ^{1}H NMR pD titration of CQ in DMSO-d_6 as a function of added $DClO_4$. (B) pKa values of the CQ protic groups, obtained by fitting the NMR chemical shift changes (Δδ) of the indicated protons as a function of pD. By lowering the pD below pKa_1, the protonation of the quinoline nitrogen causes the appearance of a new signal above 9 ppm labeled N1H.

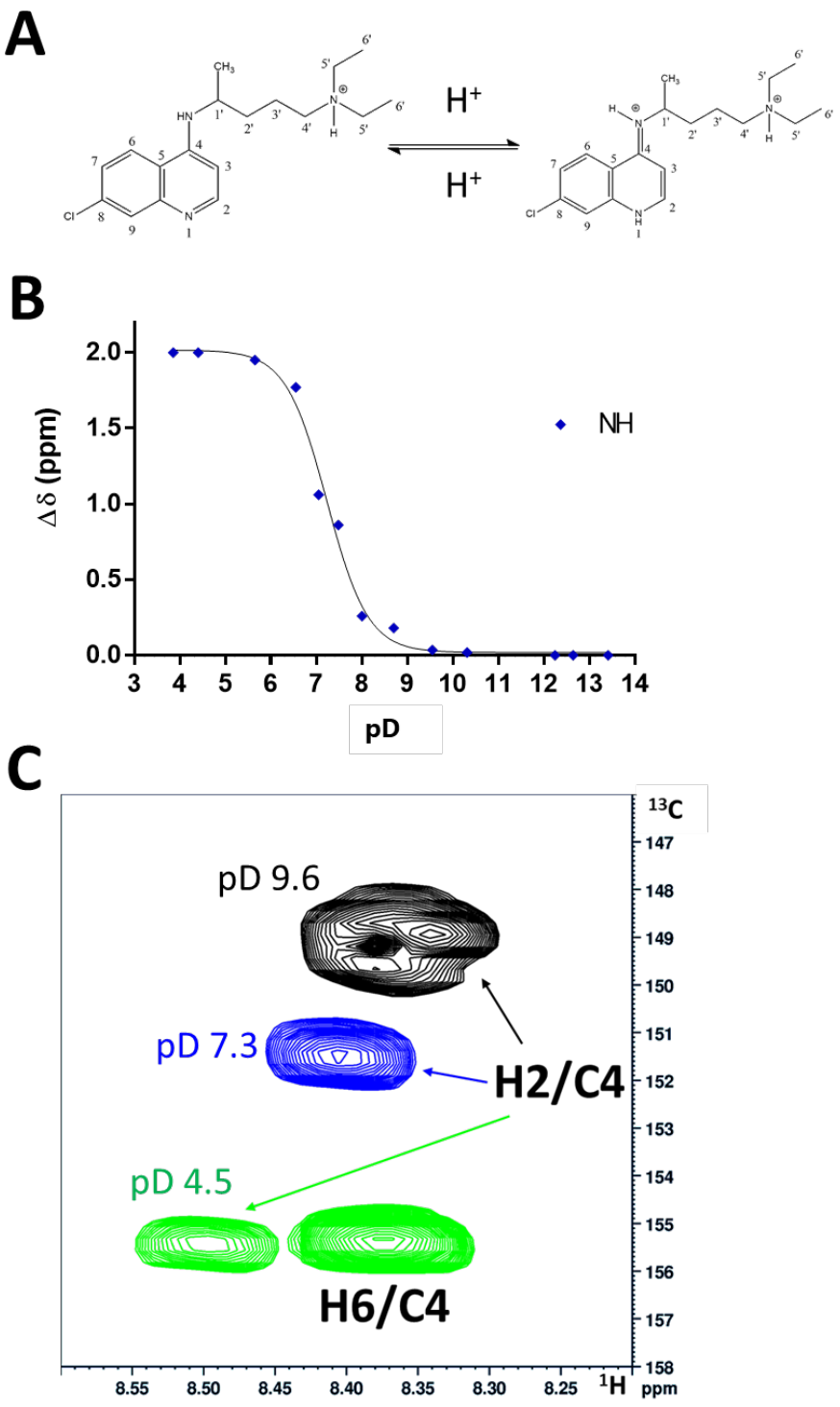

Figure S3. (A) Amino/imino tautomerism of CQ. (B) NMR chemical shift changes (Δδ) of the proton bound to the secondary aliphatic nitrogen of CQ (NH) as a function of pD; the inflection point of the interpolating curve occurs at a pD value of 7.2 (~ pKa_1). (C) Overlay of a region of 2D ^{1}H-^{13}C HMBC spectra of CQ in DMSO-d_6 at different pD values, showing the downfield shift of H2 and C4.

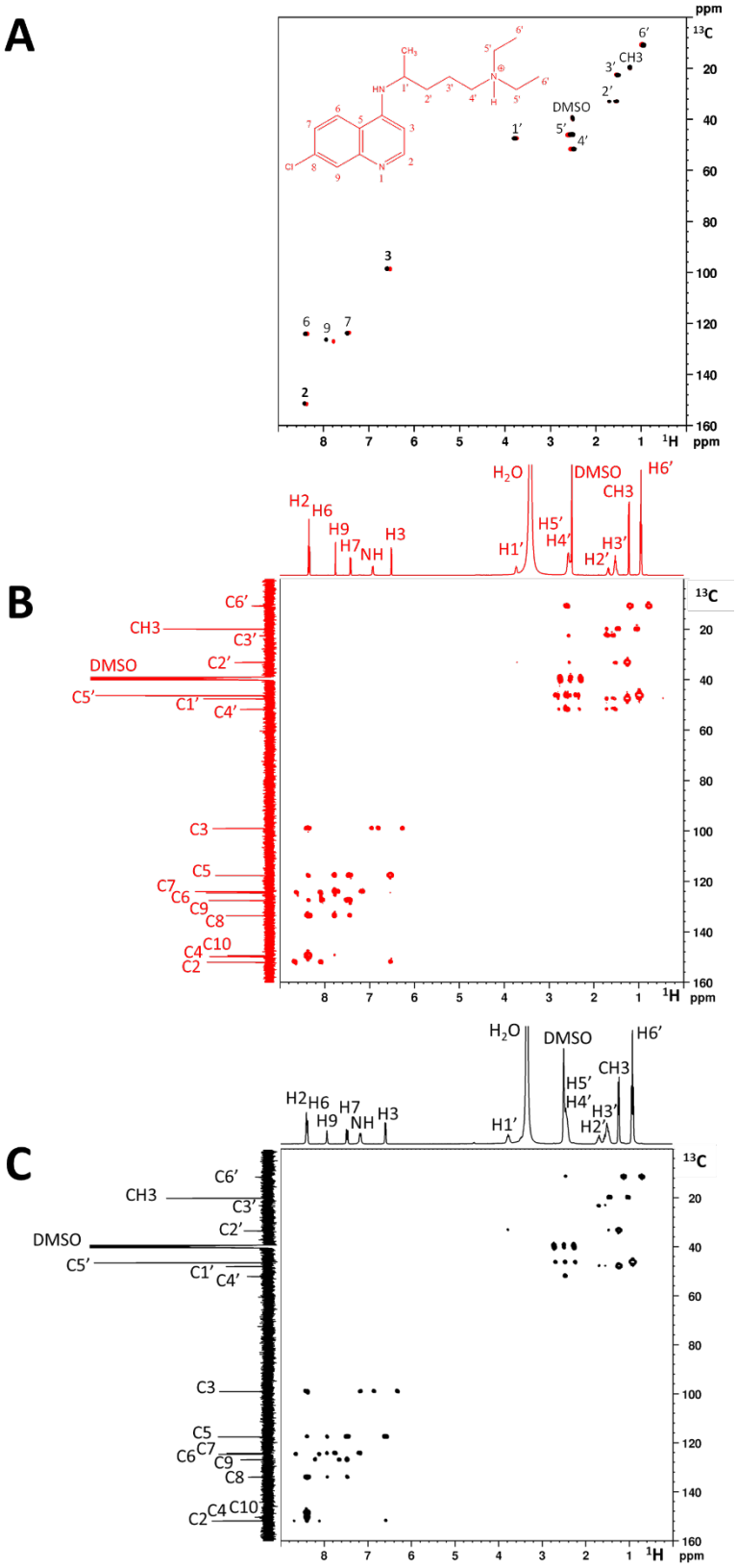

Figure S4. (A) Overlay of 2D ^{1}H-^{13}C HSQC NMR spectra of free CQ (red) and CQ with 1 equivalent of $ZnCl_2$ (black) in DMSO-d_6 (pD 9.6). The structure of CQ with atom numbering is shown as an inset. (B,C) 2D ^{1}H-^{13}C HMBC NMR spectra of free CQ (red) and CQ with 1 equivalent of $ZnCl_2$ (black) in DMSO-d_6 (pD 9.6). The assignment is reported on top of each peak in the 1D projections. The signals of residual H_2O and DMSO-d_5 are also indicated.

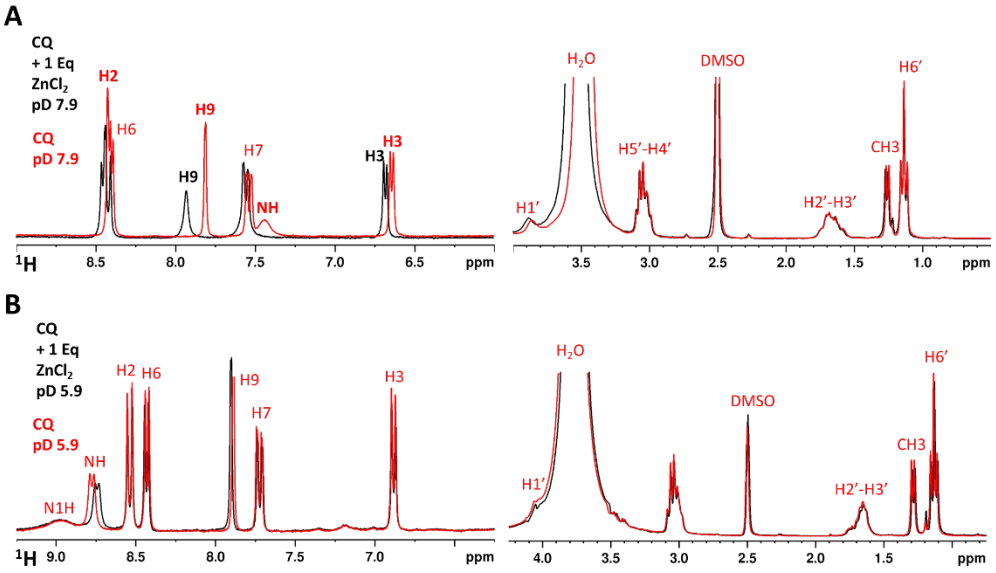

Figure S5. 1D ^{1}H NMR spectra of free CQ (red) and CQ with 1 equivalent of $ZnCl_2$ (black) in DMSO-d_6 at pD 7.9 (A) and 5.9 (B). The structure of CQ with atom numbering is shown at the top of each panel. The assignment is reported on top of each peak. The signals of residual H_2O and DMSO-d_5 are also indicated.^{1}H signals experiencing significant shifts upon Zn binding are labeled in black.

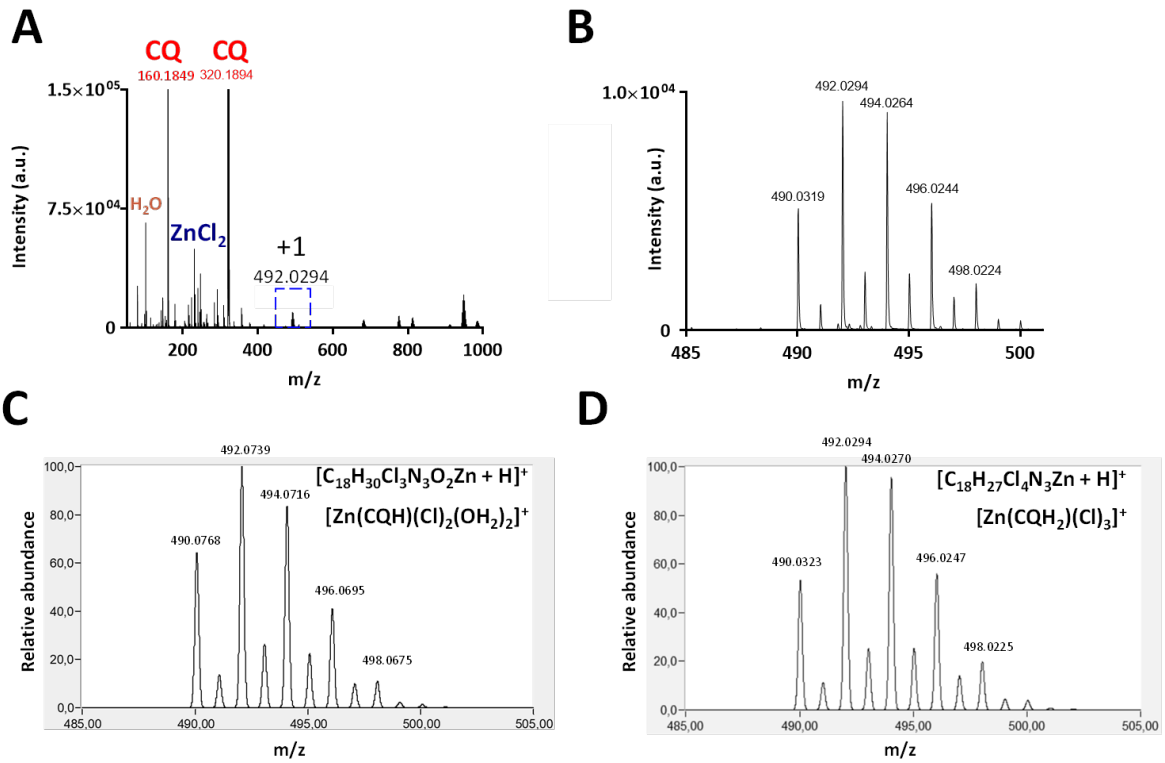

Figure S6. ESI-MS spectrum of CQ with 1 equivalent of $ZnCl_2$ in DMSO-d_6 (A) and magnification of the singly charged peak corresponding to the Zn complex (*blue dashed box*) (B). The calculated isotope mass distribution for the specified molecular formulas is shown in the lower panels (C and D).

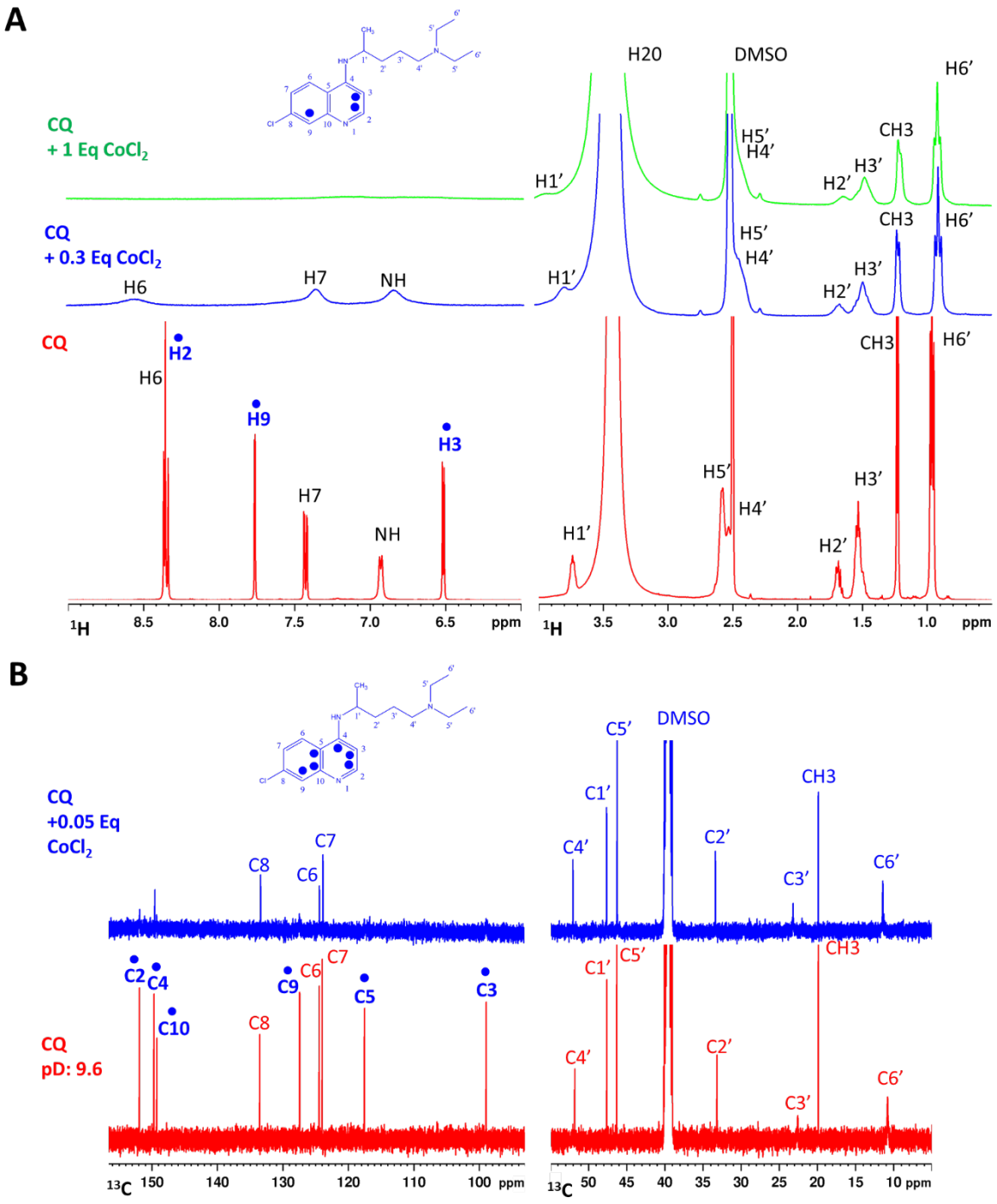

Figure S7. (A) 1D ^{1}H and (B) 1D ^{13}C NMR spectra of free CQ (red), CQ with substoichiometric amounts of $CoCl_2$ (blue) and CQ with 1 equivalent of $CoCl_2$ (green) in DMSO-d_6 (pD 9.6). The structure of CQ with atom numbering is shown at the top of each panel. ^{1}H and ^{13}C signals experiencing significant broadening upon Co^{2+} binding are marked with blue dots. The assignment is reported on top of each peak. The signals of residual H_2O and DMSO-d_5 are also indicated.

2. SINGLE CRYSTAL X-RAY DIFFRACTION

2.1 Methods

Single crystals suitable for X-ray investigation were obtained by slow evaporation of a methanol solution of chloroquine and zinc chloride. Two methanol solutions, one of racemic chloroquine and one of zinc chloride, were prepared by dissolving 2 mg of compounds in 400 µL of methanol (0.037 M for zinc chloride and 0.016 M for chloroquine). 200 µL of chloroquine solution were mixed with 120 µL of zinc chloride (chloroquine/Zn^{2+} ions molar ratio of 1:1.4). The solution was heated at 50 °C for 30 min, then 100 µL of methanol were added and the resulting solution was heated for further 15 min. The vial containing the solution was slightly unscrewed and allowed to cool slowly. Large rectangular transparent crystals were obtained after one day (Figure S8).

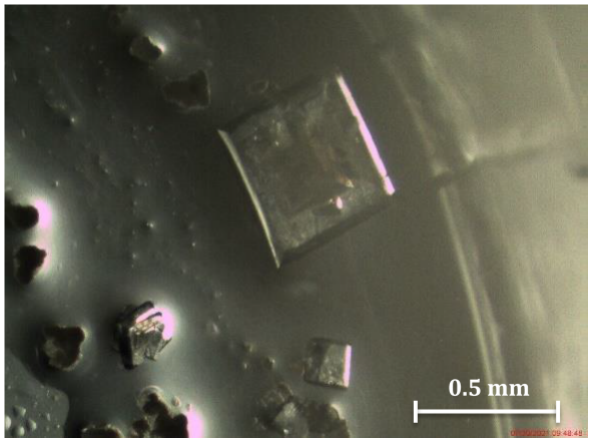

Figure S8. Single crystals of the $ZnCQCl_3$ complex.

Data collection was carried out at the XRD1 beamline of the Elettra synchrotron (Trieste, Italy), employing the rotating-crystal method with a Dectris Pilatus 2M area detector. Single crystals were dipped in Parabar 10312 cryoprotectant (from Hampton Research), mounted on a loop and flash-frozen under a nitrogen stream at a 100 K. Diffraction data were indexed and integrated using the XDS package,[2] while scaling was carried out with XSCALE.[3] The structure was solved using the SHELXT program[4] and refinement was performed with SHELXL-18/3,[5] operating through the WinGX GUI,[6] by full-matrix least-squares (FMLS) methods on F^2.

Non-hydrogen atoms were anisotropically refined. Hydrogen atoms at full occupancy were isotropically refined, while the hydrogen atoms of the disordered groups were added at calculated position and refined using the riding model. Crystallographic data and refinement details are reported in Table S1.

Table S1. Crystal data and structure refinement for tri-chloro-chloroquinium-zinc(II) complex.

	$ZnCQCl_3$
Empirical formula	$C_{18}\ H_{27}\ Cl_4\ N_3\ Zn$
Formula weight	492.59
Temperature (K)	100(2)
Wavelength (Å)	0.7
Crystal system	Orthorhombic
Space group	*P*bca
Unit cell dimensions (Å, °)	*a* = 14.439(4) *b* = 13.335(6) *c* = 22.755(5)

Volume (Å^3)	4381(3)
Z	8
r_{calcd} (g/cm^3)	1.494
m (mm^{-1})	1.610
F(000)	2032
Reflections collected	79666
Independent reflections	6521
Data / restraints / parameters	6521 / 0 / 338
GooF	1.128
Final *R* indices [I>2σ(I)]	R_1 = 0.0283 wR_2 = 0.0703
R indices (all data)	R_1 = 0.0299 wR_2 = 0.0711
CCDC code	2171746

2.2 Results

Table S2. Coordination distances and angles in the structure of $ZnCQCl_3$.

	Distances (Å)		**Angles (°)**
Zn-N(1)	2.051(1)	N(1)-Zn-Cl(2)	107.82(4)
Zn-Cl(2)	2.3086(6)	N(1)-Zn-Cl(3)	106.87(4)
Zn-Cl(3)	2.2308(8)	N(1)-Zn-Cl(4)	109.12(4)
Zn-Cl(4)	2.2746(7)	Cl(2)-Zn-Cl(3)	110.64(2)
		Cl(2)-Zn-Cl(4)	105.76(2)
		Cl(3)-Zn-Cl(4)	116.37(3)

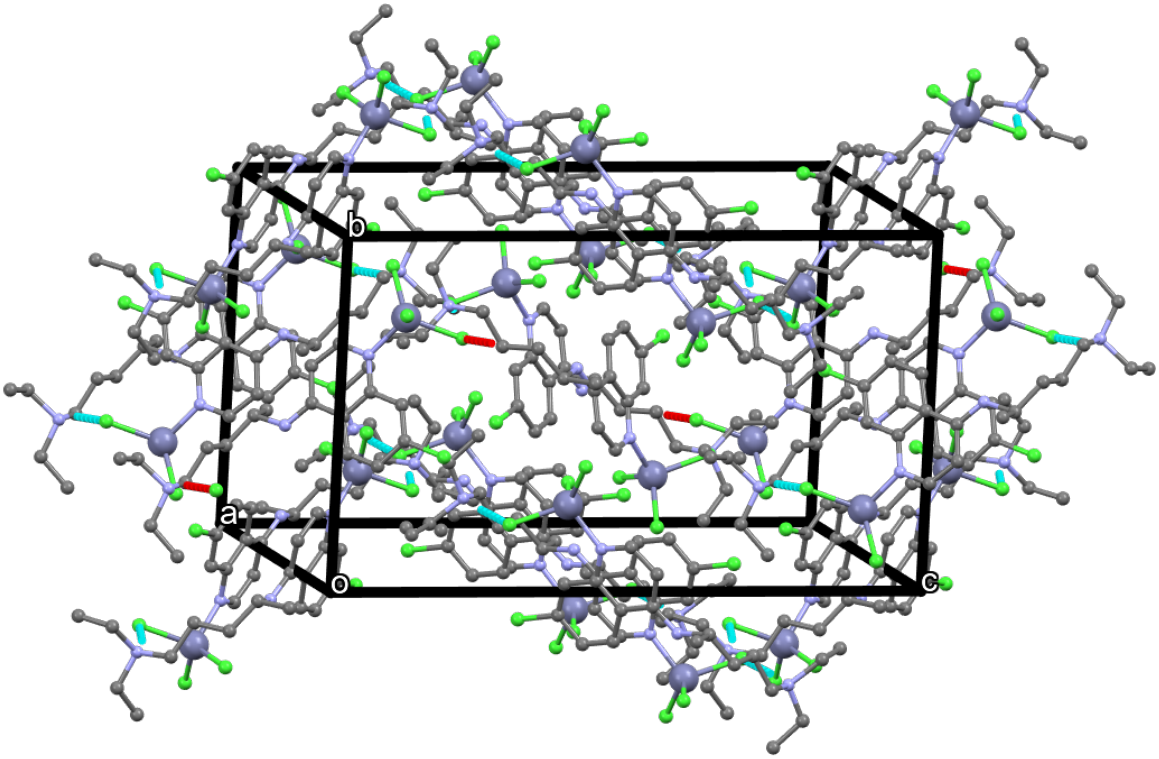

Figure S9. Crystal packing of the $ZnCQCl_3$ complex.

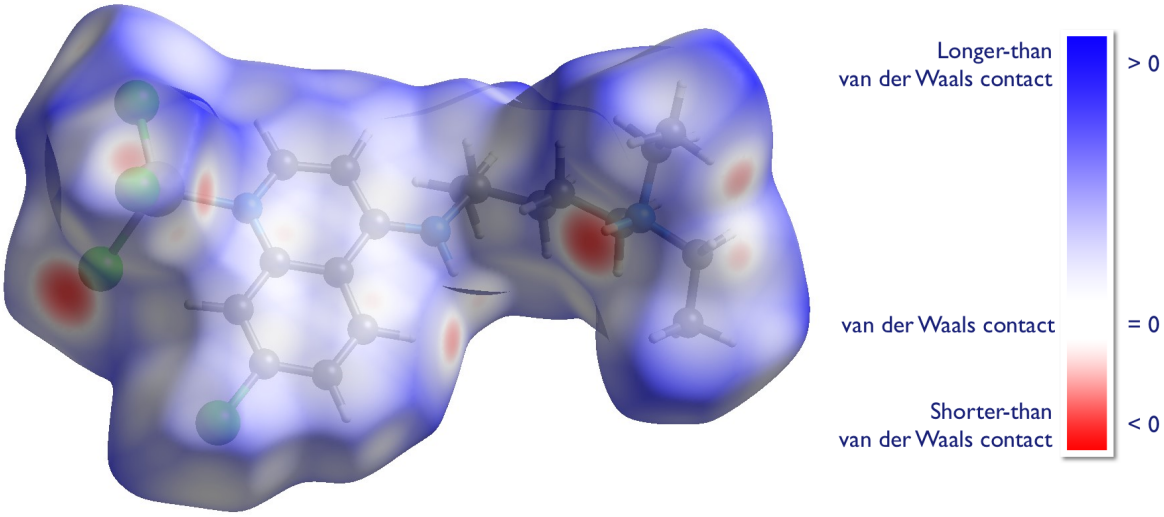

Figure S10. Hirshfeld surface of $ZnCQCl_3$ complex mapped with normalized contact distance. The red color of the surface evidences the intermolecular H-bond involving the trialkylammonium group and a coordinated chloride ion. The white color of the aromatic surface highlights the stacking interactions which stabilize the dimeric species observed in the crystal.

3. EXAFS

3.1 Results

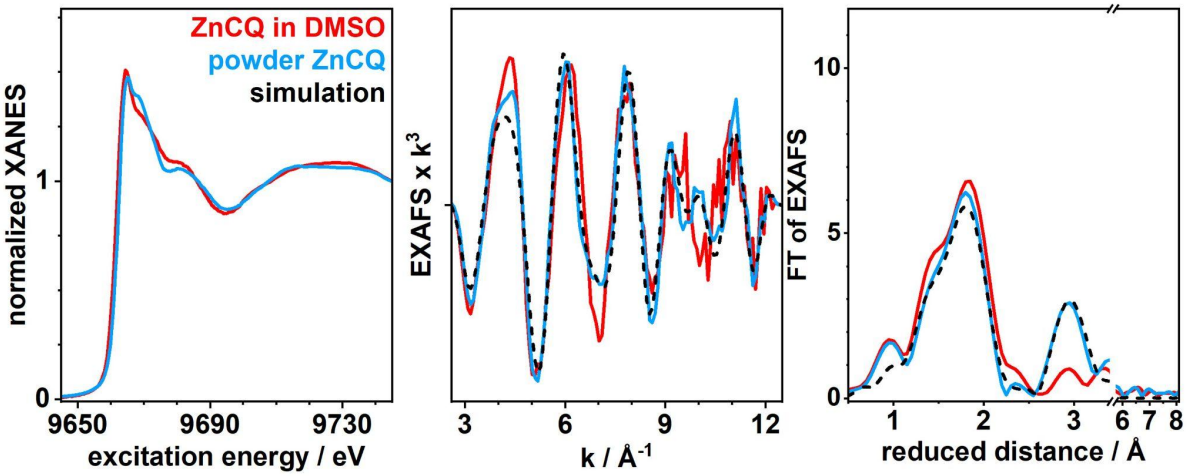

Figure S11. Zn K-edge X-ray absorption spectroscopy (XAS) of Zn-CQ frozen in DMSO-d_6 (red), Zn-CQ as powder synthesized from DMSO-d_6. Shown are normalized X-ray absorption near edge structure (XANES; left), extended X-ray absorption fine structure (EXAFS; center) and Fourier transform of EXAFS (right). Black dashed line corresponds to the EXAFS fit for the spectrum of powdered Zn-CQ using simulation parameters given in Table S3. The EXAFS fit for the Zn-CQ complex in DMSO is shown in Figure 4.

Table S3. Interatomic distances from EXAFS analysis from Zn-CQ complexes in frozen DMSO-d_6 and in crystallized form shown in Figure 4, as well as Zn-CQ and Zn-CQDP as powder synthesized from DMSO (Figures S1 and S11). Elements of the scattering shell, number of backscattering atoms in that shell (N), interatomic distance (Å) and Debye-Waller factor (σ) are listed. Atom number and Debye-Waller factor are shared between Shells as indicated, representing coordination of Zn^{2+} to the quinoline N-atom of CQ.

ZnCQ in DMSO solution				
Element	**N**	**R / Å**	**2σ² / Å²**	**Shell**
Zn-N	1	2.05	0.011	1
Zn-C	2xShell(1)	2.89	Shell(1)	2
Zn-C	Shell(1)	3.08	Shell(1)	3
Zn-O	1.18	1.92	0.004	4
Zn-Cl	1	2.24	0.009	5
Zn-Cl	1	2.25	0.007	6
Crystallised ZnCQ				
Element	**N**	**R / Å**	**2σ² / Å²**	**Shell**
Zn-N	1	2.08	0.003	1
Zn-C	2xShell(1)	2.79	Shell(1)	2
Zn-C	Shell(1)	3.08	Shell(1)	3
Zn-Cl	1	2.21	0.003	4
Zn-Cl	1	2.26	0.009	5
Zn-Cl	1	2.26	0.009	6
Zn-C	2.73	3.13	0.018	7

Zn-Cl	1.14	3.29	0.005	8
Powder ZnCQ synthesized from DMSO				
Element	**N**	**R / Å**	**$2\sigma^2$ / Å^2**	**Shell**
Zn-N	1	2.10	0.019	1
Zn-C	2xShell(1)	2.94	Shell(1)	2
Zn-C	Shell(1)	3.19	Shell(1)	3
Zn-O	1.18	1.94	0.009	4
Zn-Cl	1	2.20	0.008	5
Zn-Cl	1	2.27	0.008	6
Zn-Cl	2	3.35	0.005	7
Powder ZnCQDP synthesized from DMSO				
Zn-O	4	1.94	0.013	1
Zn-N	1	2.08	Shell(1)	2
Zn-N	2	3.34	0.003	3
Zn-C	2	3.00	0.004	4

4. AB INITIO MOLECULAR DYNAMICS

4.1 Methods

Benchmark of multiple-time step ab initio molecular dynamics. We used the $Zn(CQ_m)Cl_2(H_2O)$ structure for this benchmark. We ran 2000 BOMD steps (timestep 20 a.u.) for each timestep factor (1, 3, and 5). The trajectory sampling rate was 10. Then, we analyzed the energy fluctuations according to Eq. (8) in Ref. ([7]) We observe that a time step factor of 5 is a reasonable choice, balancing computational cost and accuracy.

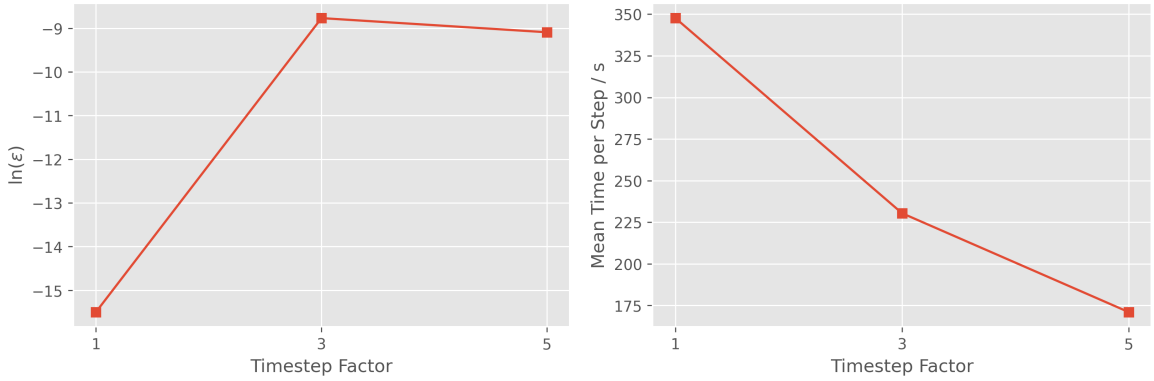

Figure S12: Energy fluctuations (plotted on a logarithmic scale) for different timestep factors (left) and the accompanying computational speedup (right).

4.2 Results

4.2.1 Averaged structural data from AIMD simulations in water solution

Table S4: Zinc coordination bond lengths (Zn–*X*) in ångström (Å) for the five complexes shown in Figure 6 of the main text. Averages were taken from 14.8 ps and 4.8 ps production runs of AIMD-BLYP and AIMD-B3LYP simulations, respectively.

Complex **CL2**			Complex **CL3**		Complex **CL**		Complex **WAT3**		Complex **WAT4**		
X	BLYP	B3LYP	*X*	BLYP	*X*	BLYP	*X*	BLYP	*X*	BLYP	B3LYP
N^{CQ}	2.07 ± 0.07	2.03 ± 0.05	N^{CQ}	2.07 ± 0.06	N^{CQ}	2.04 ± 0.06	N^{CQ}	2.02 ± 0.06	N^{CQ}	2.06 ± 0.06	2.03 ± 0.05
$Cl^{(1)}$	2.35 ± 0.09	2.30 ± 0.08	$Cl^{(1)}$	2.35 ± 0.08	$Cl^{(1)}$	2.28 ± 0.07	$O^{(1)}$	2.05 ± 0.08	$O^{(1)}$	2.28 ± 0.24	2.19 ± 0.14
$Cl^{(2)}$	2.29 ± 0.06	2.29 ± 0.08	$Cl^{(2)}$	2.37 ± 0.08	$O^{(1)}$	2.06 ± 0.08	$O^{(2)}$	2.03 ± 0.06	$O^{(2)}$	2.07 ± 0.08	2.08 ± 0.08
$O^{(1)}$	2.10 ± 0.08	2.05 ± 0.07	$Cl^{(3)}$	2.36 ± 0.08	$O^{(2)}$	2.06 ± 0.06	$O^{(3)}$	2.02 ± 0.06	$O^{(3)}$	2.20 ± 0.16	2.16 ± 0.12
—	—	—	—	—	—	—	—	—	$O^{(4)}$	2.10 ± 0.11	2.08 ± 0.12

Table S5: Zinc coordination bond angles (*X*–Zn–*Y*) in degrees for the five complexes shown in Figure 6 of the main text. Averages were taken from 14.8 ps and 4.8 ps production runs of AIMD-BLYP and AIMD-B3LYP simulations, respectively.

Complex **CL2**			Complex **CL3**		Complex **CL**		Complex **WAT3**		Complex **WAT4**		
X,*Y*	BLYP	B3LYP	*X*,*Y*	BLYP	*X*,*Y*	BLYP	*X*,*Y*	BLYP	*X*,*Y*	BLYP	B3LYP
N^{CQ},$Cl^{(1)}$	109 ± 5	110 ± 5	N^{CQ},$Cl^{(1)}$	110 ± 6	N^{CQ},$Cl^{(1)}$	118 ± 7	N^{CQ},$O^{(1)}$	110 ± 6	N^{CQ},$O^{(1)}$	94 ± 8	98 ± 8
N^{CQ},$Cl^{(2)}$	115 ± 6	113 ± 7	N^{CQ},$Cl^{(2)}$	108 ± 7	N^{CQ},$O^{(1)}$	106 ± 6	N^{CQ},$O^{(2)}$	111 ± 8	N^{CQ},$O^{(2)}$	111 ± 7	107 ± 6
N^{CQ},$O^{(1)}$	108 ± 7	108 ± 6	N^{CQ},$Cl^{(3)}$	117 ± 6	N^{CQ},$O^{(2)}$	107 ± 6	N^{CQ},$O^{(3)}$	119 ± 9	N^{CQ},$O^{(3)}$	94 ± 7	98 ± 6
$Cl^{(1)}$,$Cl^{(2)}$	114 ± 6	113 ± 7	$Cl^{(1)}$,$Cl^{(2)}$	106 ± 6	$Cl^{(1)}$,$O^{(1)}$	110 ± 7	$O^{(1)}$,$O^{(2)}$	105 ± 8	N^{CQ},$O^{(4)}$	132 ± 9	131 ± 11
$Cl^{(1)}$,$O^{(1)}$	103 ± 6	105 ± 7	$Cl^{(1)}$,$Cl^{(3)}$	109 ± 6	$Cl^{(1)}$,$O^{(2)}$	110 ± 7	$O^{(1)}$,$O^{(3)}$	106 ± 8	$O^{(1)}$,$O^{(2)}$	88 ± 7	86 ± 5
$Cl^{(2)}$,$O^{(1)}$	105 ± 7	106 ± 7	$Cl^{(2)}$,$Cl^{(3)}$	106 ± 6	$O^{(1)}$,$O^{(2)}$	102 ± 7	$O^{(2)}$,$O^{(3)}$	102 ± 6	$O^{(1)}$,$O^{(3)}$	164 ± 7	161 ± 8
—	—	—	—	—	—	—	—	—	$O^{(1)}$,$O^{(4)}$	83 ± 8	84 ± 5
—	—	—	—	—	—	—	—	—	$O^{(2)}$,$O^{(3)}$	96 ± 7	91 ± 7
—	—	—	—	—	—	—	—	—	$O^{(2)}$,$O^{(4)}$	113 ± 11	121 ± 13
—	—	—	—	—	—	—	—	—	$O^{(3)}$,$O^{(4)}$	86 ± 7	85 ± 6

Table S6: Overall potential energies in Hartree (E_h) for the five complexes shown in Figure 6 of the main text. Averages were taken from the 14.8 ps production runs of AIMD-BLYP simulations. Note that for complex **CL3** one solvent water molecule was replaced by a sodium ion to neutralize the system. Thus, the comparison among these values is not straightforward.

Complex **CL2**	Complex **CL3**	Complex **CL**	Complex **WAT3**	Complex **WAT4**
-2111.414 ± 0.045	-2136.944 ± 0.036	-2111.411 ± 0.027	-2111.435 ± 0.032	-2111.395 ± 0.031

4.2.2 Electronic Density and Electrostatic Potential Map

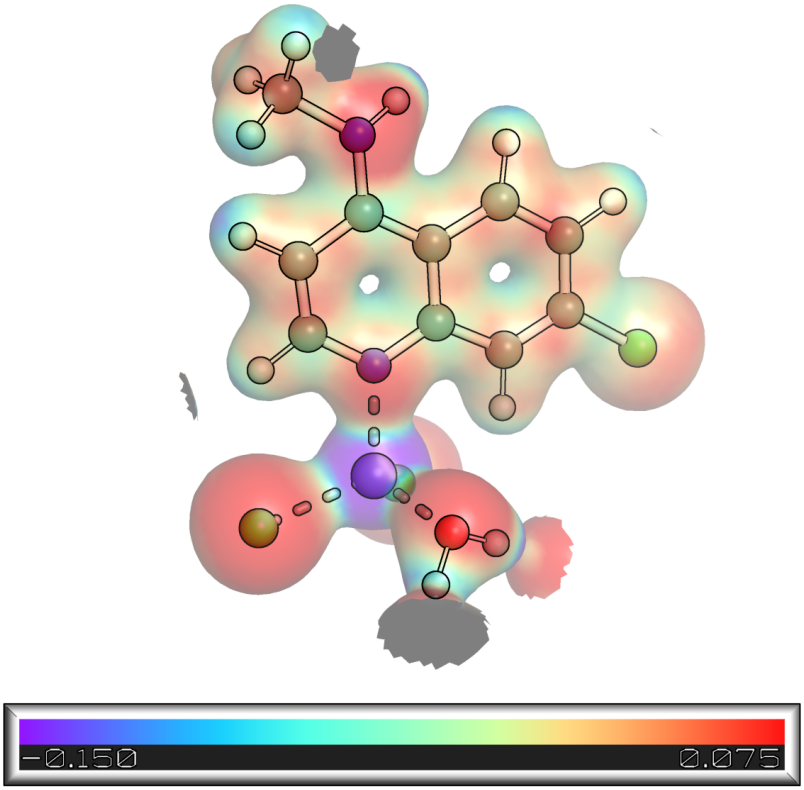

Figure S13: Electrostatic potential (in Hartree·e^{-1}) projected onto the electron density isosurface (density level = 0.03 e·bohrs^{-3}) of complex **CL2** from an AIMD-BLYP snapshot in aqueous solution. Note the electron density of the surrounding solvent hydrogen bonded to the coordinating water molecule.

4.2.3 Calculated NMR Chemical Shifts

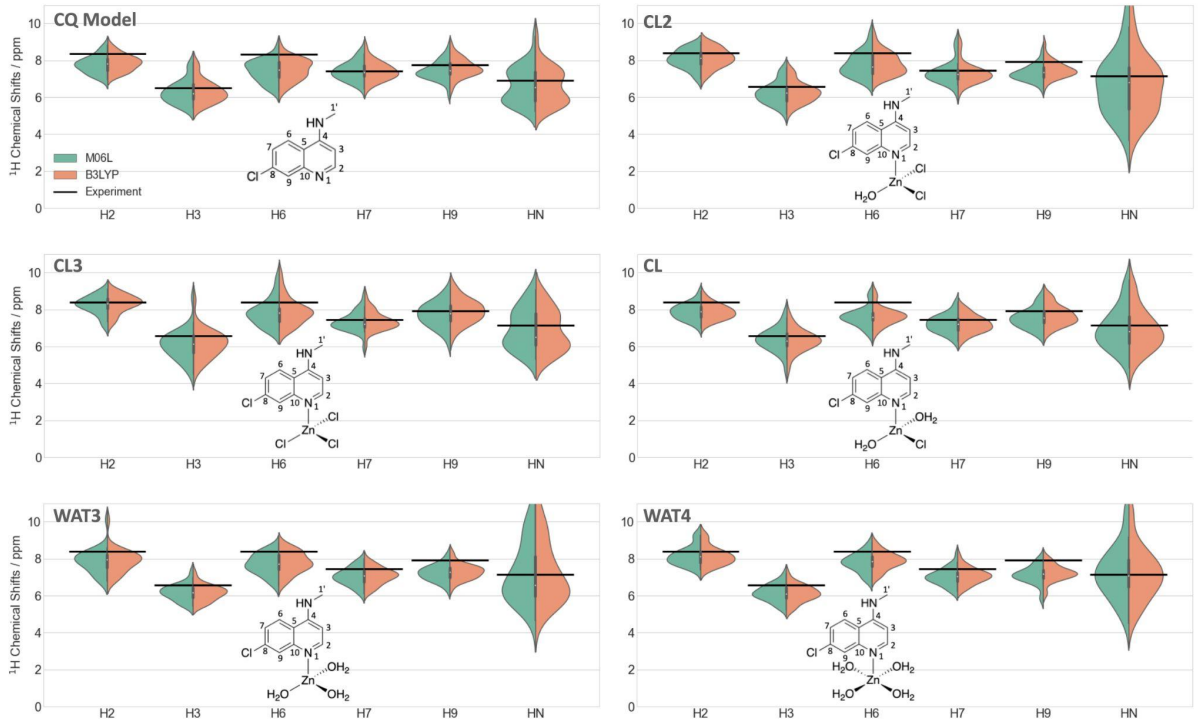

Figure S14: Calculated ^{1}H NMR chemical shift distributions using DFT with M06L[8] and B3LYP[9,10], compared with experimental data (black lines). The corresponding systems are shown as structural formulas.

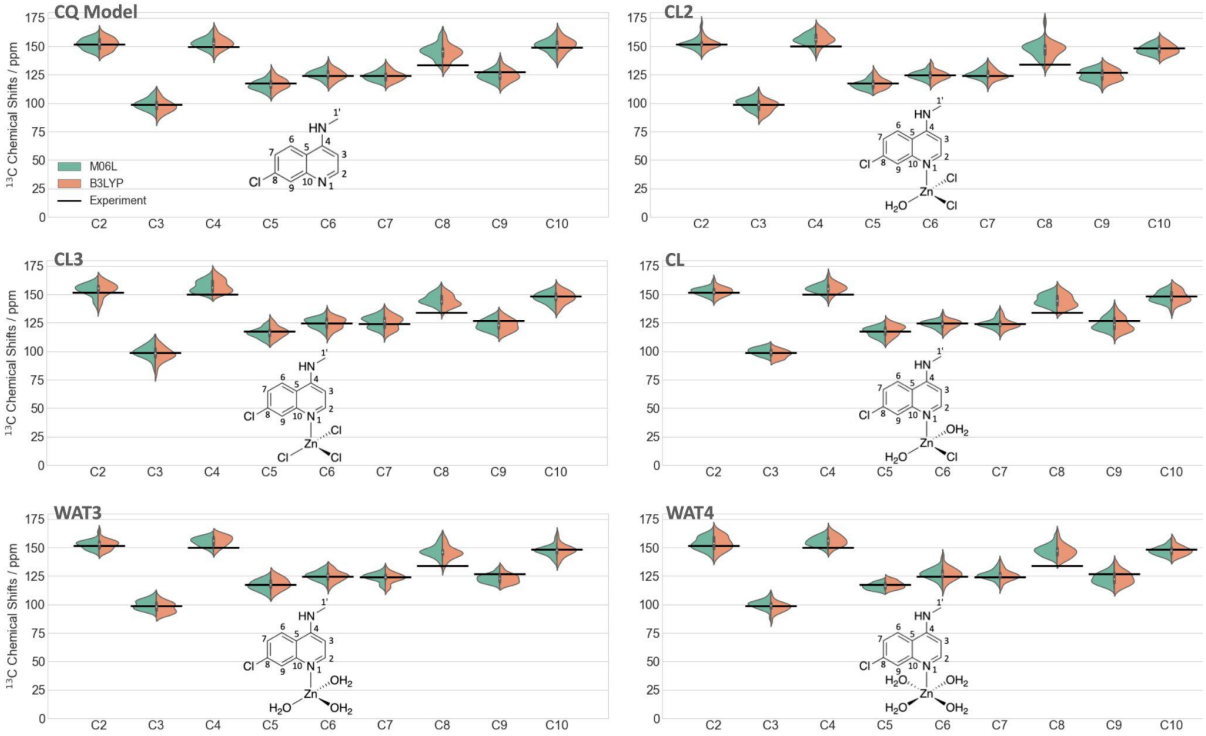

Figure S15: Calculated ^{13}C NMR chemical shift distributions using DFT with M06L[8] and B3LYP[9,10], compared with experimental data (black lines). The corresponding systems are shown as structural formulas.

4.2.4 Simulated EXAFS spectra in water solution

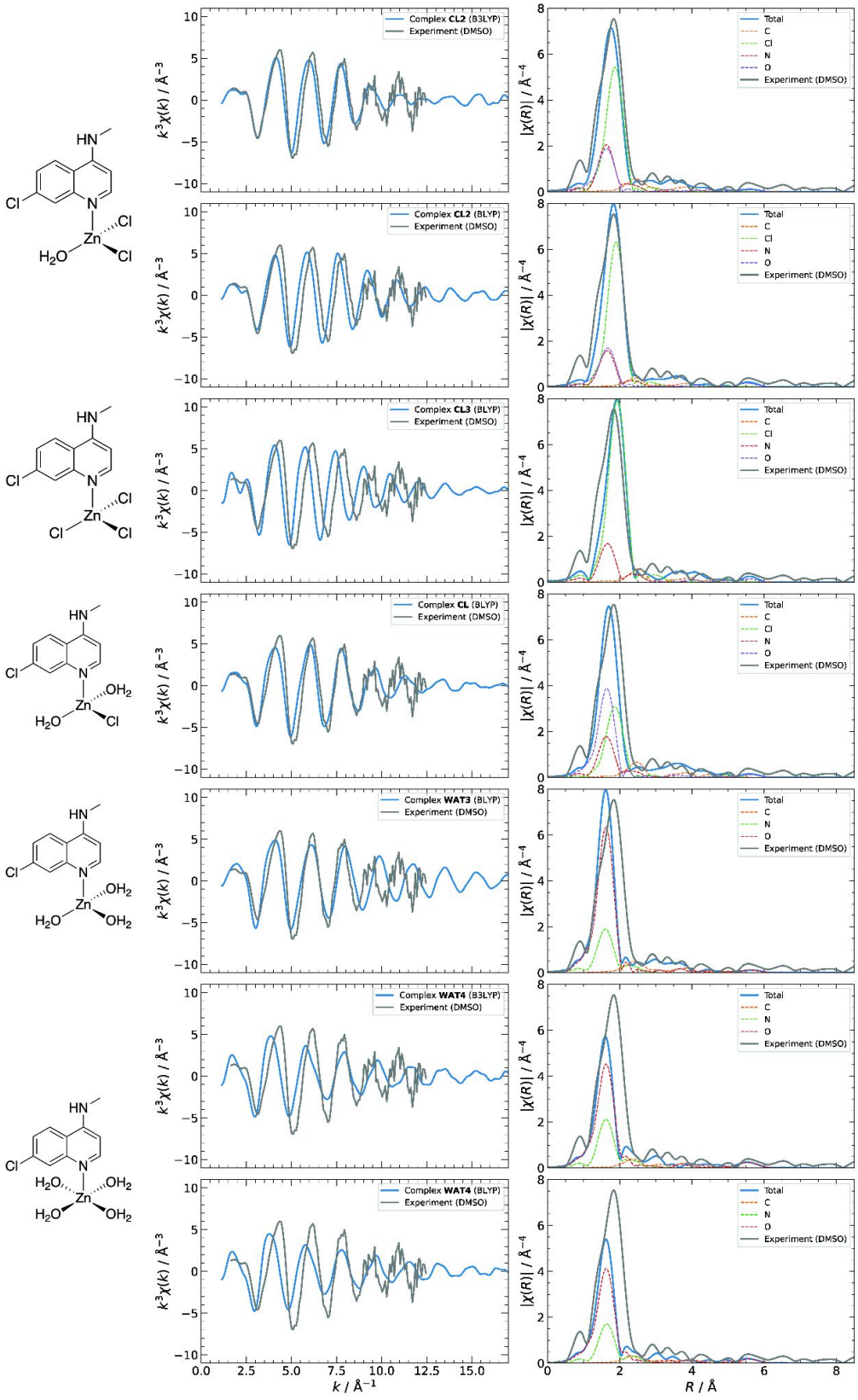

Figure S16: Left: Configurational averaged k^3-weighted EXAFS spectra of the five different complexes in water solution from 300 [100] equidistant snapshots of the 14.4 ps AIMD-BLYP [4.8 AIMD-B3LYP] simulation. Comparison is made with the experimental spectrum recorded in frozen DMSO solution. Right: The corresponding Fourier transforms of the k3-weighted EXAFS spectra (same coloring schemes). Atom specific contributions are also included.

5. QUANTUM CHEMISTRY CALCULATIONS

5.1 Methods

The structures and energetics of the penta-coordinated $[Zn(CQH)Cl_2(H_2O)_2]^+$ and tetra-coordinated $[Zn(CQH)Cl_2(H_2O)]^+$ with an dissociated water molecule in the gas phase were calculated at the B3LYP-D3(BJ)/def2-TZVP level of theory.[9–13] Hereby, the aliphatic side chain was considered explicitly and modeled in its protonated state at the tertiary nitrogen. The geometries were optimized. Frequency analysis ensured the convergence to true minima. Electronic energies were then determined at the DLPNO-CCSD(T1) level of theory,[14,15] extrapolating between the def2-SVP and def2-TZVPP basis after the scheme in Ref. ([16]). Thermal, rotational and vibrational contributions to the molecular free energies were considered at the DFT level. Additionally, molecular solvation free energies were determined through the SMD implicit solvation model.[17] Hereby, geometries were re-optimized with the same electronic structure method as for gas phase optimizations. DLPNO-CCSD(T1)/def2-TZVPP calculations with the SMD water model were compared to the gas phase results, where their difference provided an estimate for the solvation-free energy. Finally, the comparison of reaction free energies in the different phases required the contribution of 7.9 kJ·mol^{-1} for the change of the reference states in the gas phase (298 K; 1 atm) and in solution (298 K; 1 mol·L^{-1}). All calculations were carried out with the ORCA 5.0.1 program package.[18]

5.2 Results

Mass spectrometry (MS) suggests that the complex is tetra-coordinated with the molecular formula $[Zn(CQH_2)Cl_3]^+$ while the $[Zn(CQH)Cl_2(H_2O)_2]^+$ complex was originally proposed by Navarro *et al*.[1] The latter coordination environment was not stable in the AIMD simulations in water (see main text), and led readily to the $[Zn(CQH)Cl_2(H_2O)]^+$ complex by dissociating a water molecule. Here we optimized the geometry of these tetra- and penta-coordinated species in the gas phase and in solution (using an implicit solvent model, Figure S16). Molecular free energies (derived from thermochemical analysis at 298 K) estimated the relative stability under the different conditions.

The B3LYP optimized structures of the tetra-coordinated species revealed an interesting feature on passing from the gas phase to the solution (see Figure S16(a–b)). The Cl–Zn–Cl angle is hereby significantly reduced from 134.9° in the gas phase to 118.8° using the implicit solvent model (which is in reasonable agreement with the averaged angle of 113° ± 7° from the AIMD simulations). This contraction arises because of the weaker ionic interactions between the polarized chloride ions in solution. In fact, a vacant coordination site is formed in the gas phase, which could be filled by a water molecule upon evaporation to generate a penta-coordinated complex. The optimized structure of this penta-coordinated complex, in which the ligands are positioned in *trans* configurations, turns out to be very similar to that of the same complex in implicit water solvent (Figure S16(c–d)). The calculation of molecular free energies from these models gives us insights for the relative stability of the complexes in the gas phase and in solution. The associated water dissociation free energies support the idea of varying coordination numbers in the different media: While water dissociation of a penta-coordinated complex in the gas phase is unfavored by +8.9 kJ·mol^{-1}, the dissociation of one water molecule is driven by a decrease of the free energy of –22.9 kJ·mol^{-1} under solution conditions. These results additionally cross-validate our observations from AIMD simulations in explicit solvent.

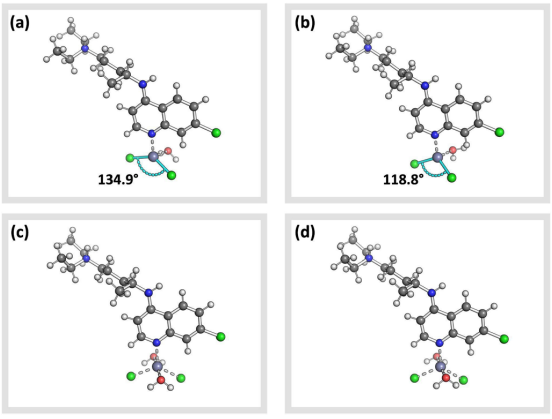

Figure S17: B3LYP optimized structures of Zn-CQ complexes in the gas phase and in aqueous solution using an implicit solvent model. (a) Tetra-coordinated Zn-CQ ligated with two chloride ions and one water molecule in the gas phase. (b) Tetra-coordinated Zn-CQ ligated with two chloride ions and one water molecule in solution. (c) Penta-coordinated Zn-CQ ligated with two chloride ions and two water molecules in the gas phase. (d) Penta-coordinated Zn-CQ ligated with two chloride ions and two water molecules in solution.

6. REFERENCES

(1) Navarro, M.; Goitia, H.; Silva, P.; Velásquez, M.; Ojeda, L. E.; Fraile, G. Synthesis and Characterization of New Copper– and Zinc–Chloroquine Complexes and Their Activities on Respiratory Burst of Polymorphonuclear Leukocytes. *J Inorg Biochem* **2005**, *99* (8), 1630–1636. https://doi.org/10.1016/j.jinorgbio.2005.05.002.

(2) Kabsch, W. *XDS*. *Acta Crystallogr D Biol Crystallogr* **2010**, *66* (2), 125–132. https://doi.org/10.1107/S0907444909047337.

(3) Kabsch, W. Integration, Scaling, Space-Group Assignment and Post-Refinement. *Acta Crystallogr D Biol Crystallogr* **2010**, *66* (2), 133–144. https://doi.org/10.1107/S0907444909047374.

(4) Sheldrick, G. M. *SHELXT* – Integrated Space-Group and Crystal-Structure Determination. *Acta Crystallogr A Found Adv* **2015**, *71* (1), 3–8. https://doi.org/10.1107/S2053273314026370.

(5) Sheldrick, G. M. Crystal Structure Refinement with *SHELXL*. *Acta Crystallogr C Struct Chem* **2015**, *71* (1), 3–8. https://doi.org/10.1107/S2053229614024218.

(6) Farrugia, L. J. *WinGX* and *ORTEP for Windows*: An Update. *J Appl Crystallogr* **2012**, *45* (4), 849–854. https://doi.org/10.1107/S0021889812029111.

(7) Liberatore, E.; Meli, R.; Rothlisberger, U. A Versatile Multiple Time Step Scheme for Efficient Ab Initio Molecular Dynamics Simulations. *J Chem Theory Comput* **2018**, *14* (6), 2834–2842. https://doi.org/10.1021/acs.jctc.7b01189.

(8) Zhao, Y.; Truhlar, D. G. A New Local Density Functional for Main-Group Thermochemistry, Transition Metal Bonding, Thermochemical Kinetics, and Noncovalent Interactions. *J Chem Phys* **2006**, *125* (19), 194101. https://doi.org/10.1063/1.2370993.

(9) Becke, A. D. Density-functional Thermochemistry. III. The Role of Exact Exchange. *J Chem Phys* **1993**, *98* (7), 5648–5652. https://doi.org/10.1063/1.464913.

(10) Stephens, P. J.; Devlin, F. J.; Chabalowski, C. F.; Frisch, M. J. Ab Initio Calculation of Vibrational Absorption and Circular Dichroism Spectra Using Density Functional Force Fields. *J Phys Chem* **1994**, *98* (45), 11623–11627. https://doi.org/10.1021/j100096a001.

(11) Grimme, S.; Antony, J.; Ehrlich, S.; Krieg, H. A Consistent and Accurate Ab Initio Parametrization of Density Functional Dispersion Correction (DFT-D) for the 94 Elements H-Pu. *Journal of Chemical Physics* **2010**, *132* (15). https://doi.org/10.1063/1.3382344.

(12) Grimme, S.; Ehrlich, S.; Goerigk, L. Effect of the Damping Function in Dispersion Corrected Density Functional Theory. *J Comput Chem* **2011**, *32* (7), 1456–1465. https://doi.org/10.1002/jcc.21759.

(13) Weigend, F.; Ahlrichs, R. Balanced Basis Sets of Split Valence, Triple Zeta Valence and Quadruple Zeta Valence Quality for H to Rn: Design and Assessment of Accuracy. *Physical Chemistry Chemical Physics* **2005**, *7* (18), 3297. https://doi.org/10.1039/b508541a.

(14) Riplinger, C.; Pinski, P.; Becker, U.; Valeev, E. F.; Neese, F. Sparse Maps—A Systematic Infrastructure for Reduced-Scaling Electronic Structure Methods. II. Linear Scaling Domain Based Pair Natural Orbital Coupled Cluster Theory. *J Chem Phys* **2016**, *144* (2), 024109. https://doi.org/10.1063/1.4939030.

(15) Guo, Y.; Riplinger, C.; Becker, U.; Liakos, D. G.; Minenkov, Y.; Cavallo, L.; Neese, F. Communication: An Improved Linear Scaling Perturbative Triples Correction for the Domain Based Local Pair-Natural Orbital Based Singles and Doubles Coupled Cluster Method [DLPNO-CCSD(T)]. *J Chem Phys* **2018**, *148* (1), 011101. https://doi.org/10.1063/1.5011798.

(16) Liakos, D. G.; Neese, F. Improved Correlation Energy Extrapolation Schemes Based on Local Pair Natural Orbital Methods. *Journal of Physical Chemistry A* **2012**, *116* (19), 4801–4816. https://doi.org/10.1021/jp302096v.

(17) Marenich, A. v.; Cramer, C. J.; Truhlar, D. G. Universal Solvation Model Based on Solute Electron Density and on a Continuum Model of the Solvent Defined by the Bulk Dielectric Constant and Atomic Surface Tensions. *J Phys Chem B* **2009**, *113* (18), 6378–6396. https://doi.org/10.1021/jp810292n.

(18) Neese, F. The ORCA Program System. *WIREs Computational Molecular Science* **2012**, *2* (1), 73–78. https://doi.org/10.1002/wcms.81.